Modified UiO-66 frameworks with methylthio, thiol and sulfonic acid function groups: The structure and visible-light-driven photocatalytic property study

Teng-Fei Chen[a], Shu-Yan Han[a], Zhi-Peng Wang[a], Hui Gao[a], Lin-Yang Wang[a], Yu-Heng Deng[a], Chong-Qing Wan[a,b,*], Yang Tian[a], Qiang Wang[c], Guo Wang[a,*], Gui-Sheng Li[d,*]

[a] Department of Chemistry, Capital Normal University, Beijing 100048, China
[b] State Key Laboratory of Structural Chemistry, Fujian Institute of Research on the Structure of MatterChinese Academy of Sciences, Fuzhou, Fujian 350002, China
[c] Elementary Education College, Capital Normal University, Beijing 100048, China
[d] The Education Ministry Key Lab of Resource Chemistry, Shanghai Key Laboratory of Rare Earth Functional MaterialsShanghai Normal University, Shanghai 200234, China

ARTICLE INFO

ABSTRACT

Isostructural **UiO-66-(SO$_3$H)$_2$**, **UiO-66-(SH)$_2$** and **UiO-66-(SCH$_3$)$_2$** were obtained through systemic synthesis by decorating the sulfur-containing groups (X = –SCH$_3$, –SH, –SO$_3$H) on the terephthalate linkers of UiO-66 (a metal-organic framework constructed with terephthalate linkers and Zr(IV)-oxo clusters). These UiO-66-X$_2$ derivates exhibited as n-type semiconductors, wherein the electronic properties and molecule dimensions of the function groups –X played key roles in determining their band gap (E$_g$) and photoactive properties. The –SCH$_3$ is shown as the most efficient functional group and is responsible for that dramatically narrowed E$_g$ of the **UiO-66-(SCH$_3$)$_2$** and photocatalytic property. In sharp contrast to that state-of-the-art UiO-66-NH$_2$ (constructed with 2-aminoterephthalate linkers) having no visible-light induced photocatalytic activity to split water into H$_2$ even with Pt as co-catalyst, Pt/**UiO-66-(SCH$_3$)$_2$** showed a high efficient H$_2$ generation (3871 µmol/g) from water with sacrificial ascorbic acid (0.2 M) under λ > 400 nm irradiation. The structure-property relationship of UiO-66-X$_2$ was studied through experimental and theoretical methods.

1. Introduction

Exploring new visible-light-driven photocatalysts with high solar energy conversion is one of the most attractive topics to reduce environmental contamination and address energy problems [1]. Due to the large band gap of many known photocatalysts (e.g. TiO$_2$), only UV light with small proportion energy of solar spectrum can be used [2]. Rationally narrowing the band gap of a semiconductor-type photocatalyst is viewed as the promising method to produce new type of photocatalyst that can absorb the light region with extended wavelength to visible light, realizing more solar-energy utilization with high efficiency. Many relevant efforts are devoted to rationally design and synthesize various new materials such as doped metal chalcogenides [3a-c], dye-sensitized systems [3d,e] and nanomaterials [3f,g] etc. to achieve these objectives.

Metal-organic frameworks (MOFs) are crystalline complexes featuring 3D framework built up through coordination bonds between inorganic building units (metal ions or clusters) and organic linkers [4]. Peoples find MOF can exhibit semiconductor behaviors. The photogenerated electrons from the organic linkers can transfer to the metal-oxo clusters, exhibiting a linker-to-cluster charge-transfer (LCCT) process [5],[6]. Band gap of a MOF's material can thus be artificially adjusted through varying and/or decorating the organic linkers, thus realizing the beneficial photoactivity such as visible-light response and improved photoactivities. Modifying the organic linkers on a MOF structure is commonly and successfully used method for this proposing. The –NH$_2$ has been evidenced as the most efficient functional group to narrowe the band gap of a given MOF as compared to other groups such as –Br, − OH, –SH and –NO$_2$ till now [7]. The typical sample is UiO-66-NH$_2$ [6a], a MOF constructed with 2-aminoterephthalate linkers and Zr(IV)-oxo clusters, which has a markedly narrowed band gap upon amino functionalizing as compared to its parent UiO-66 (containing terephthalate linker, Fig. 1) [6b], leading to a much bathochromic-shifted spectrum. Another representative amino-functionalized sample

Fig. 1. Synthesis diagram of isostructural **UiO-66-(SH)$_2$**, **UiO-66-(SCH$_3$)$_2$** and **UiO-66-(SO$_3$H)$_2$** possessing the parent structure of UiO-66. The octahedral cage represents the pore structure within UiO-66-X$_2$.

is MIL-125-NH$_2$, a MOF derived from 2-aminoterephthalate linkers and Ti(IV)-oxo clusters, which showed much improved photoactivities (CO$_2$ reduction [6c] and H$_2$ prodcution [6d]) driven by visible light due to the narrowed band gap with respect to that of patent MIL-125. However, Zr(IV)-UiO-66-NH$_2$ has no visible-light-induced photocatalytic activity to split water into H$_2$ even with Pt as co-catalyst [7]. Very recently, a new methylthio –SCH$_3$ was introduced on terephthalate linker by ours group to achieve a photoactive MOF's material x%-MIL-125-(SCH$_3$)$_2$ [8]. The H$_2$ evolution rate of the new visible-light-driven catalyst was improved to 10 times that of the reported MIL-125-NH$_2$ [6d]. It is believed that the –SCH$_3$ modified on the terephthalate linkers attributed to that markedly narrowed band gap and significantly improved H$_2$ evolution rate of the new type of MIL-125-based material.

In terms of extending -SCH$_3$ group to other families of MOFs and further investigating the influence of sulfur-containing groups, isostructural complexes UiO-66-X$_2$ with the terephthalate linkers modified by various X groups (X = –SH, –SCH$_3$, –SO$_3$H) were obtained through systemic synthesis (Fig. 1). Experimental and theoretic studies were performed and elucidated the significant effect of the electronic nature, molecule dimension and geometry of the –X groups on the photoactive properties of UiO-66-X$_2$. To our pleasant surprise, the –SCH$_3$ was evidenced as the most efficient functional group to achieve the photocatalytic Zr(IV)-UiO-66 system with H$_2$ generation ability from water. **Pt/UiO-66-(CH$_3$)$_2$** with Pt as co-catalyst exhibited the better stability and high H$_2$ generation (3871 μmol/g) as the ascorbic acid acted as the sacrificial reagent (0.2 M) under visible-light irritation (λ > 400 nm), showing almost no hydrogen-evolution decay even after 3 cycle reactions of 3 h.

2. Result and discussion

UiO-66 family is chosen in this study because their frameworks are thermal stable [6b,9] and tolerable to many solvents including aqueous solution with a wide pH range [10], which will make sure of the UiO-66-X$_2$ as stable photocatalyst candidates. H$_2$BDC-(SH)$_2$ (2,5-dimercaptoterephthalic acid) [11] and H$_2$BDC-(SCH$_3$)$_2$ (2,5-bis(methylthio)terephthalic acid) [8] were obtained following the procedures reported, while **UiO-66-(SH)$_2$** and **UiO-66-(SCH$_3$)$_2$** were synthesized through a same method as that for UiO-66 by use the H$_2$BDC-(SH)$_2$ and

H$_2$BDC-(SCH$_3$)$_2$ as the linkers, respectively (see ESI, Fig. 1). With regard to **UiO-66-(SO$_3$H)$_2$**, a reported UiO-66 derivate with sulfonic acid groups (-SO$_3$H) at 2,5-position on the terephthalate linkers, was obtained by oxidizing the -SH groups on UiO-66-(SH)$_2$ via postsynthetic modification [12]. These isostructured UiO-66-X$_2$ (X= –SH, –SCH$_3$, –SO$_3$H) derivates were characterized via powder X-ray diffractions (PXRD). As shown in Fig. 2a, the identical XRD patterns of UiO-66 and UiO-66-X$_2$ indicate these derivates have the same 3D porous crystalline lattices as that of parent UiO-66, featuring hexanuclear zirconium oxyhydroxide clusters (Zr$_6$O$_4$(OH)$_4$(R−CO$_2$)$_{12}$) and octahedral cages assembled with these modified terephthalate linkers (Fig. 1). The 2,5-positions of terephthalate linkers of each UiO-66-X$_2$ are modified with –SH for **UiO-66-(SH)$_2$**, -SO$_3$H for **UiO-66-(SO$_3$H)$_2$** and -SCH$_3$ groups for **UiO-66-(SCH$_3$)$_2$** with their parent UiO-66 frameworks remained intact [6b].

N$_2$ adsorption/desorption isotherms of desolvated UiO-66-X$_2$ were measured to assess the architectural stability and permanent porosity of UiO-66-X$_2$. The measured Brunauer − Emmett − Teller (BET) show N$_2$ gas adsorption of 712 m^2/g, 488 m^2/g and 284 m^2/g for **UiO-66-(SH)$_2$**, **UiO-66-(SCH$_3$)$_2$** and **UiO-66-(SO$_3$H)$_2$**, respectively (Fig. 2b, Table S1), and the micropore volumes of corresponding MOFs are 0.24 cm^3/g, 0.14 cm^3/g and 0.07 cm^3/g, respectively. These values are relative lower than that of parent UiO-66 (1069 m^2/g, 0.45 cm^3/g) [6b]. These facts indicate that the -SH, -SCH$_3$ and -SO$_3$H groups protrude into the micropores of the isostructure complexes UiO-66-X$_2$, leading to their decreased pore volume and BET values as compared to these of their parent UiO-66. The pore size values of UiO-66-X$_2$ also are accordingly changed upon the presence of various –X groups (X = –SH, –SCH$_3$, –SO$_3$H) (Fig. S1). These varied pore volume and BET values follow the same order as that of Van del Waals volumes of the –X groups (V$_{-SH}$ < V$_{-SCH3}$ < V$_{-SO3H}$) [9a]. The larger molecular dimension of a –X group (X= –SH, –SCH$_3$, –SO$_3$H), the smaller pore volume and BET values of a UiO-66-X$_2$ obtained (Table S1).

Solid FT-IR spectra of the activated UiO-66-X$_2$ samples were measured and shown in Fig. 2c. The S−H groups functioned on the terephthalate linkers of **UiO-66-(SH)$_2$** show the stretching vibration peak at 2572 cm^{-1}. For **UiO-66-(SCH$_3$)$_2$**, the vibration band of C−H around 2934 cm^{-1} for the −CH$_3$ group suggests the BDC-(SCH$_3$)$_2$ linkers on the MOF. As regards that for **UiO-66-(SO$_3$H)$_2$**, the asymmetrical and

(a)

(b)

(c)

(d)

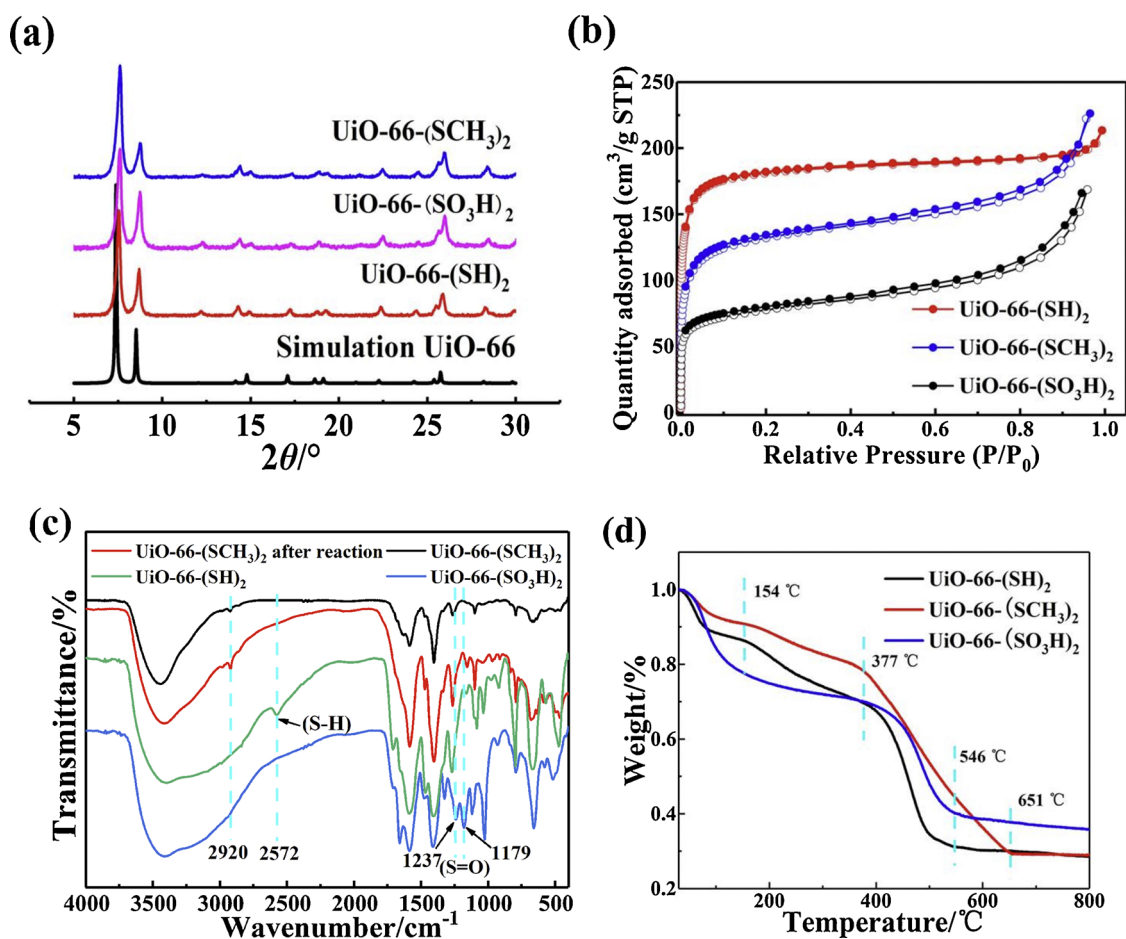**Fig. 2.** PXRD (a), N_2 adsorption isotherms (b), FT-IR spectra (c) and thermogravimetric analysis (d) for **UiO-66-(SH)$_2$, UiO-66-(SCH$_3$)$_2$** and **UiO-66-(SO$_3$H)$_2$**. Simulated PXRD patterns of UiO-66 are obtained from its crystal data[9b].

symmetrical vibrational peaks of O = S=O are found at $1237 cm^{-1}$ and $1179 cm^{-1}$, respectively. Meanwhile, the absent stretching vibration peak of –SH at $2572 cm^{-1}$ indicates that the –SH groups on **UiO-66-(SH)$_2$** have all been oxidized into –SO$_3$H groups, leading to the post-synthesized **UiO-66-(SO$_3$H)$_2$**. From the thermogravimetric (TG) analysis of the as-made UiO-66-X$_2$ (Fig. 2d), we can see their different weight loss with temperature increasing. **UiO-66-(SO$_3$H)$_2$** exhibits two steps with the first loss of the DMF guest within the pores before 154 °C and the second loss of the decomposed linkers with the onset temperature at 400 °C. For **UiO-66-(SH)$_2$** and **UiO-66-(SCH$_3$)$_2$**, there are three weight loss steps upon heating. The evacuations of the absorbed DMF completed before 154 °C with different mass percents, then the second weight losses occurred between 154 °C and 377 °C range. These second weight losses can be explained by the partially decomposing of H$_2$BDC-(SH)$_2$ or H$_2$BDC-(SCH$_3$)$_2$ for **UiO-66-(SH)$_2$** and **UiO-66-(SCH$_3$)$_2$**, respectively. The weight loss end up to 546 °C for **UiO-66-(SH)$_2$** and **UiO-66-(SO$_3$H)$_2$**, and to 651 °C for **UiO-66-(SCH$_3$)$_2$**, with their structures collapsed to produce the metal oxide ZrO$_2$.

Interestingly, upon modifying the aromatic ring of terephthalate linkers on **UiO-66-X$_2$** with different − X groups UV − vis spectra of solid state **UiO-66-(SH)$_2$, UiO-66-(SCH$_3$)$_2$** and **UiO-66-(SO$_3$H)$_2$** exhibit distinct plots (Fig. 3a). Contrast to these main absorption bands within the UV region (edge of 320 nm) of their parent UiO-66, the band edges of **UiO-66-(SO$_3$H)$_2$, UiO-66-(SH)$_2$** and **UiO-66-(SCH$_3$)$_2$** are around 425, 440 and 470 nm, respectively. Such absorptions broadened to visible-light region of the sulfur-containing UiO-66-X$_2$ are consistent with their yellow color changed from that white of UiO-66 (Fig. 3a). The red shift of these UiO-66-X$_2$ with respect to that spectra of UiO-66 follow the order **UiO-66-(SO$_3$H)$_2$ < UiO-66-(SH)$_2$ < UiO-66-(SCH$_3$)$_2$**,

with **UiO-66-(SCH$_3$)$_2$** having the most intense absorption band from 320 nm to 470 nm (center at 420 nm), which can be ascribed to linker-to-cluster charge transfer mechanism (LCCT) [5ab,6a]. The functioned − X groups with distinct electronic properties have an increasing electronic effect on the aromatic ring of the terephthalate linkers of UiO-66-X$_2$, engendering their various absorptions within the visible-light region (Fig. 3a). Hammett constant σ_m values of 0.15, 0.25 and 0.55 for − SCH$_3$, −SH and − SO$_3$H, respectively, suggest electron-donating abilities of − X groups follow the order of − SCH$_3$ > − SH > − SO$_3$H [7a,13]. Such order linearly correlates with the red-shift order for UV–vis spectra of UiO-66-X$_2$. So, the − X group with a larger electron-donating capacity to the aromatic linker may be beneficial, which results in a higher level of the highest occupied molecular orbital that thus markedly narrows the band gap (E$_g$) [5ab,6a,8] of UiO-66-X$_2$, leading to the much red shift of **UiO-66-(SCH$_3$)$_2$**. Optical band gaps calculated for UiO-66-X$_2$ through the equation $(Ah\nu)^2 = \alpha(h\nu\ E_g)$ and UV–vis absorption diagrams further confirm this point of view. As shown in Table S2 and Fig S4, the measured band gap values are 2.80 eV, 3.02 eV and 3.22 eV for **UiO-66-(SCH$_3$)$_2$, UiO-66-(SH)$_2$** and **UiO-66-(SO$_3$H)$_2$)**, respectively, being much lower than that 4.0 eV of the parent UiO-66 [7bc]. Obviously, it is the different − X groups modified on the terephthalate linkers of the MOF's frameworks lead to their distinct E$_g$ values of the UiO-66-X$_2$. Moreover, the experiment gap of **UiO-66-(SCH$_3$)$_2$** (2.80 eV) is comparable to that of UiO-66-NH$_2$ (2.72 eV, mono-substituted –NH$_2$ on the terephthalate linker) [7c], although the electron-donating ability of − NH$_2$ is much larger than that of − SCH$_3$ due to the smaller Hammett constant σ_m value -0.16 of − NH$_2$ [7a,13]. This fact may be explained by the disubstituted function group effect of **UiO-66-(SCH$_3$)$_2$**.
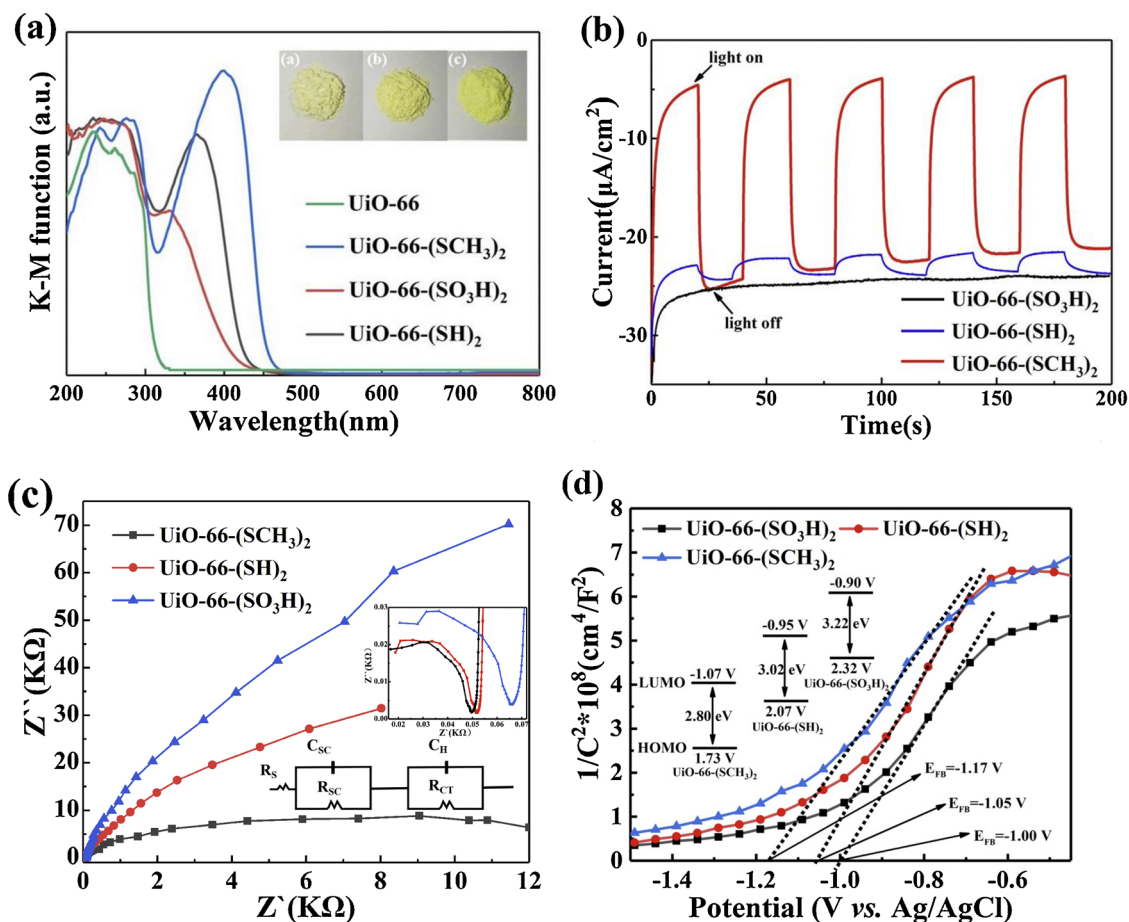
Fig. 3. (a) UV–vis absorption spectra of UiO-66-X$_2$ in this study. (b) Current/time plots of UiO-66-X$_2$ measured at an applied bias potential of 0.19 V vs. RHE with and without visible-light irradiation (> 400 nm) pulse of 20 s. (c) Nyquist and (d) Mott − Schottky plots of UiO-66-X$_2$ in 0.1 M H$_2$SO$_4$.

With the aim to gain a deep insight into the electronic properties of the modified UiO-66-X$_2$, theoretical calculations were carried out. The hybrid density functional HSE06 [14], which can accurately describe the band gaps of solids [15], was adopted. Consistent TZVP basis sets [16,17] optimized for solids were used. Since the lattice parameter is larger than 20 Å, a $2 \times 2 \times 2$ k-points sampling was used in the first Brillouin zone. All the calculations were performed by using the CRYSTAL14 program [18]. The structure of UiO-66 was investigated firstly. The optimized lattice constant of the cubic cell is 20.75 Å, which is quite close to the experimental value 20.78 Å in literature [9b]. The energies of the highest occupied crystal orbital (HOCO) at the valence band maximum and the lowest unoccupied crystal orbital (LUCO) at the conduction band minimum are -6.60 and -2.29 eV, respectively. Thus the band gap is 4.31 eV, being close to the measured experimental value 4.0 eV [7bc]. **UiO-66-(SH)$_2$** was also investigated with the same method. The –SH groups were manually added to the UiO-66 structure, and no significant blockade between groups was found. After adding the –SH groups, the symmetry breaks down. Thus only the atomic coordinates of the –SH groups were further optimized due to the huge computational resources required (more than five hundreds atoms per unit cell contains). The energies of the HOCO and LUCO are -4.69 and -2.43 eV, respectively. Thus, the band gap is dramatically decreased to 2.26 eV with respect to that 4.31 eV of UiO-66, being lower than the experimental optical band gap of 3.02 eV (Fig. S3 and Table S2). Notably, both of the HOCO and LUCO are spread mainly on the benzene rings, and the bonds in the HOCO are more than that in the LUCO (Fig. 4ab). Modified the –SH groups on the benzene rings, p-π conjugation occurs between the sulfur atoms and the benzene rings in the HOCO (Fig. 4c). However, such sulfur atoms contribute little to the LUCO of **UiO-66-**

(SH)$_2$, thus the LUCO (-2.43 eV) of which is similar to that of UiO-66 (-2.29 eV) (Fig. 4d). While, the HOCO of **UiO-66-(SH)$_2$** change significantly from -6.60 to -4.69 eV, leading to that significantly decreased band gap of 2.26 eV as compared to that 4.31 eV of UiO-66. Regarding the –SCH$_3$ and –SO$_3$H groups whose molecular dimensions are much larger than that of –SH group, significant blockage occurs as the models were manually built. No symmetry can be utilized, and the full geometrical optimization is not applicable due to the huge computational resources required. As the HOCO and LUCO are mainly on the linkers BDC-X$_2$ of the MOFs, calculation based on the single molecule model of BDC-X$_2$ can directly reflect those band gaps of UiO-66-X$_2$. This is confirmed by the fact that the calculated energy gap's order of BDC (4.89 eV) > BDC-(SO$_3$H)$_2$ (4.68 eV) > BDC-(SCH$_3$)$_2$ (3.01 eV) > BDC-(SH)$_2$ (2.90 eV) is almost in accordance with their optical band gap order of UiO-66 (4.07 eV) > **UiO-66-(SO$_3$)$_2$** (3.22 eV) > **UiO-66-(SH)$_2$** (3.02 eV) > **UiO-66-(SCH$_3$)$_2$** (2.80 eV) (Fig. S3 and Table S2). The slight difference from the experiment E$_g$ is the calculated gap of BDC-(SO$_3$)$_2$ (4.68 eV) only decreasing a little as compared to that of BDC-(SH)$_2$ (4.89 eV); while, the experiment E$_g$ (3.22 eV) of **UiO-66-(SO$_3$)$_2$** markedly decreased as compared to that 4.07 eV of UiO-66. Herein, the bigger van der Waals volume of the –SO$_3$H significantly affects the geometries and then the electronic properties of **UiO-66-(SO$_3$)$_2$** bearing an ordered 3D architecture, which may accounts for that markedly decreased E$_g$ of **UiO-66-(SO$_3$)$_2$**. That large groups would exhibit strong stereo effect on the linkers and then on the coordination geometry of the Zr(IV)-oxo clusters, although the **UiO-66-(SO$_3$)$_2$** maintains the topology of UiO-66 [9b]. The different order of the energy gap BDC-(SCH$_3$)$_2$ (3.01 eV) > BDC-(SH)$_2$ (2.90 eV) from that of **UiO-66-(SH)$_2$** (3.02 eV) > **UiO-66-(SCH$_3$)$_2$** (2.80 eV) can also be ascribed to the
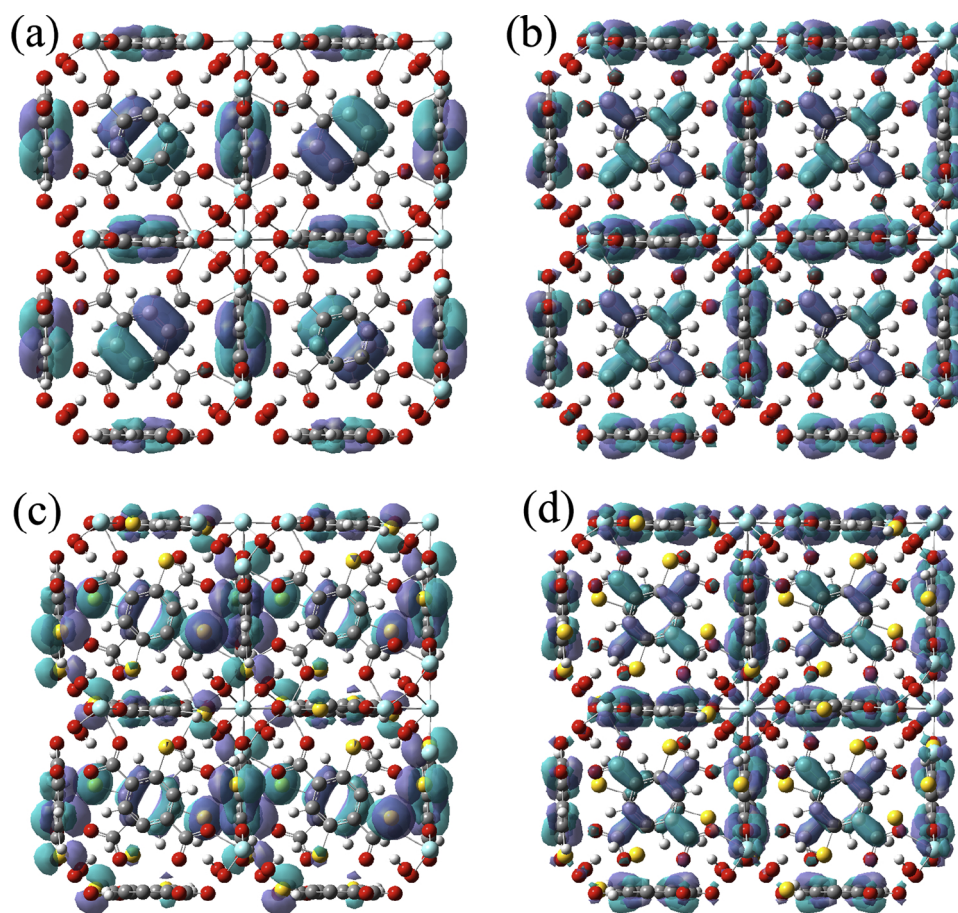
Fig. 4. (a) HOCO and (b) LUCO of UiO-66, (c) HOCO and (d) LUCO of **UiO-66-(SH)$_2$**.

various molecular dimension effect of function groups –X on the 3D structural UiO-66-X$_2$. These narrowed band gaps of UiO-66-X$_2$ upon –X modification are similar to those decreased E_g values observed for other UiO-66-X (X = $-NH_2$, $-NO_2$, $-Br$, $-OH$) complexes [7].

For further investigating the photo-responsive property, photoelectrochemical tests under the irradiation of a filtered light ($\lambda > 400\,nm$) from Xenon lamp were performed with metal Pt as the counter electrode and Ag/AgCl as the reference electrode (ESI). The liner sweep voltammetry curves of UiO-66-X$_2$ (X = $-SO_3H$, $-SH$, $-SCH_3$) are shown in Fig. S3. **UiO-66-(SCH$_3$)$_2$** shows obvious current change under dark and light conditions within the visible range ($\lambda > 400\,nm$), indicating that **UiO-66-(SCH$_3$)$_2$** is sensitive to visible light and generates a large amount of photoelectrons under the visible light irradiation. In comparison, **UiO-66-(SH)$_2$** shows less current change under on-off such irradiations, inferring the weaker response to the visible light ($\lambda > 400\,nm$) than that of **UiO-66-(SCH$_3$)$_2$**. In sharp contrast to **UiO-66-(SCH$_3$)$_2$**, **UiO-66-(SO$_3$H)$_2$** exhibits an ignorable response to such irradiation. These current-time curves for UiO-66-X$_2$ infer their different photocurrent responsive abilities following the order of **UiO-66-(SCH$_3$)$_2$** > (˜19.67 μA·cm^{-2}) > **UiO-66-(SH)$_2$** (˜0.82 μA/cm^{-2}) > **UiO-66-(SO$_3$H)$_2$** (˜0 μA/cm^{-2}) (Fig. 3b). This order correlates well with the largest red shift of the spectrum of **UiO-66-(SCH$_3$)$_2$** (edge of 470 nm) and the least shift of **UiO-66-(SO$_3$H)$_2$** (edge of 425 nm) (Fig. 3a). Also, such results are consistent with their optical band gap order of 3.22 eV, 3.02 eV, 2.80 eV for **UiO-66- (SO$_3$H)$_2$**, **UiO-66-(SH)$_2$** and **UiO-66-(SCH$_3$)$_2$**, respectively (Table S2, Fig S4).

Distinct photocurrents of UiO-66-X$_2$ (X = $-SO_3H$, $-SH$, $-SCH_3$) reflect their different interface charge separation efficiencies. To further evidence this point of view, electrochemical impedance spectroscopy was measured to view the interfacial properties between the electrode

and electrolyte. As shown in Fig. 3c, the capacitance arc measured for **UiO-66-(SCH$_3$)$_2$** is much smaller than that of **UiO-66-(SH)$_2$** and **UiO-66-(SO$_3$H)$_2$**, suggesting the highest electron mobility and a lowest electron-hole recombination rate for **UiO-66-(SCH$_3$)$_2$** [19a]. Moreover, Mott-Schottky (M–S) plots (ESI) acquired by impedance spectroscope (performed at an AC frequency of 1 KHz to) is shown in Fig. 3d, indicating an n-type semiconductor for UiO-66-X$_2$ due to positive slopes of these plots. The flat band position (E_{FB}) values calculated through Mott-Schottky equation[19bc] at $1/C^2 = 0$ (ESI) are -1.00 V, -1.05 V and -1.17 V vs. Ag/AgCl (i.e. -0.81 V, -0.86 V and -0.98 V vs NHE) for **UiO-66-(SO$_3$H)$_2$**, **UiO-66-(SH)$_2$** and **UiO-66-(SCH$_3$)$_2$** (Fig. 3d), respectively. Thus, conductor band (CB) of UiO-66-X$_2$ are correspondingly estimated to be -0.90 V and -0.95 V and -1.07 V vs. NHE, respectively. Based on the band gap values of UiO-66-X$_2$ (X = $-SO_3H$, $-SH$, $-SCH_3$) 3.22 eV, 3.02 eV and 2.80 eV (Fig. S3), respectively, their corresponding valence band (VB) thus are 2.32 V for **UiO-66-(SO$_3$H)$_2$**, 2.07 V for **UiO-66-(SH)$_2$** and 1.73 V for **UiO-66-(SCH$_3$)$_2$** vs. NHE (Fig. 3d).

Visible-light driven hydrogen ($\lambda > 400\,nm$) production from aqueous solution by use UiO-66-X$_2$ (X = $-SO_3H$, $-SH$, $-SCH_3$) as photocatalysts were conducted. Parallel experiments of UiO-66-X$_2$ samples were carried out by suspending the solid samples (50 mg) in deionized water (80 mL) containing 0.1 vol% triethanolamine (TEOA) as a sacrificial reagent. No H$_2$ evolution was observed for all cases. While, as 1.5 wt% platinum was loaded as a co-catalyst [20], three Pt/UiO-66-X$_2$ exhibited different visible-light driven hydrogen generation rates. The H$_2$ evolution measured after 1 h are 0 μmol/g, 2.97 μmol/g and 6.96 μmol/g for Pt/**UiO-66-(SO$_3$H)$_2$**, Pt/**UiO-66-(SH)$_2$** and Pt/**UiO-66-(SCH$_3$)$_2$**, respectively. Obviously, in sharp contrast to that state-of-the-art UiO-66-NH$_2$ that has no photocatalytic activity driven by visible light [6d], herein **UiO-66-(SCH$_3$)$_2$** and **UiO-66-(SH)$_2$** acted as a visible-
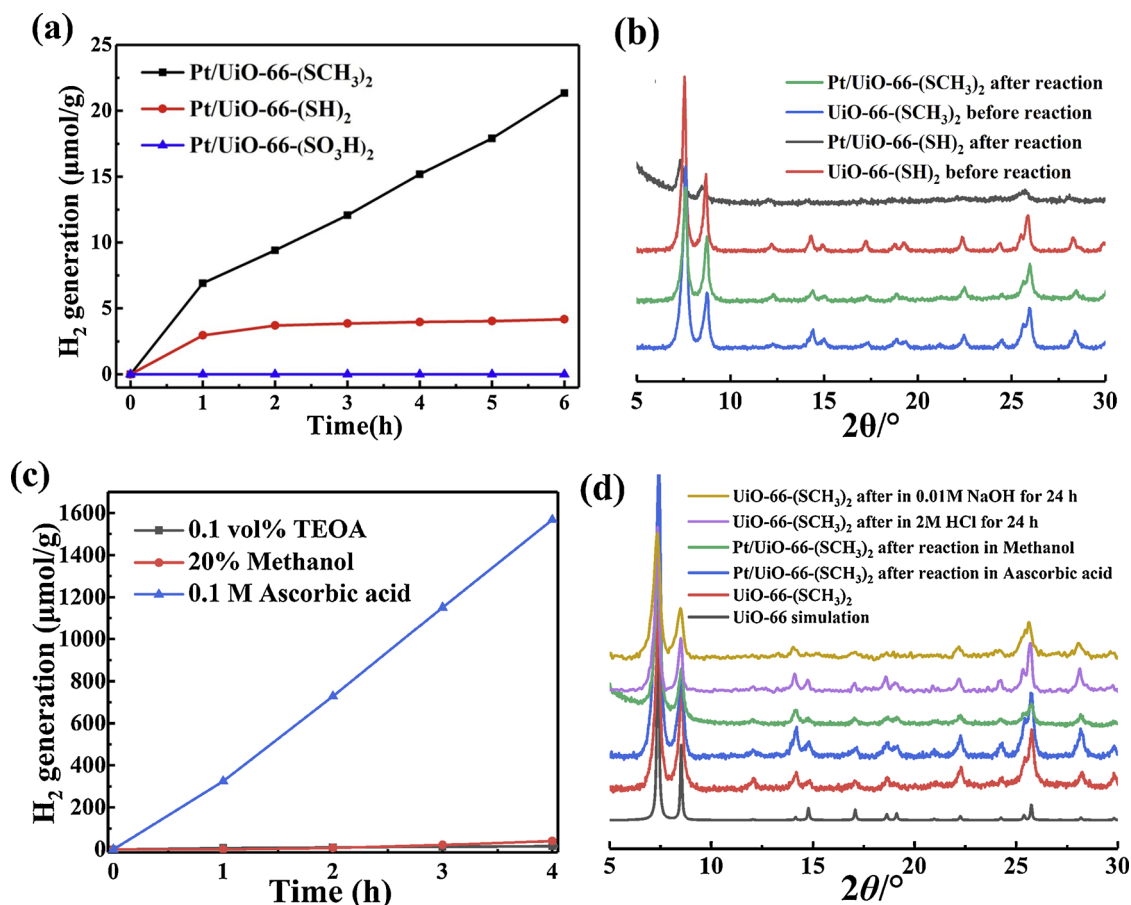
Fig. 5. (a) Time course of H_2 production of Pt/UiO-66-X_2 from aqueous solution with 0.1 vol% TEOA as electronic sacrificial reagent at room temperature, and PXRD of which before and after reaction (b). (c) Time course of H_2 production of Pt/UiO-66-$(SCH_3)_2$ with 0.1 M ascorbic acid, 20 vol% methanol and 0.1 vol% TEOA as sacrificial electron donors in comparison. (d) PXRD patterns comparison after reactions and soaking in different pH solution.

light driven photocatalyst to splitting water into H_2. Time course of photocatalytic hydrogen production for 6 h are displayed and compared in Fig. 5a. Pt/**UiO-66-(SCH₃)₂** exhibited stable H_2 generation and the total production reached 17.86 μmol/g after 6 h. While, no more hydrogen generated in the next 3 h for Pt/**UiO-66-(SH)₂**. Compared PXRD of the samples before and after photocatalytic reactions shows that the patterns of **UiO-66-(SCH₃)₂** are almost unchanged, while the diffraction peaks of **UiO-66-(SH)₂** are markedly weaken after reaction (Fig. 5b). These fact indicate **UiO-66-(SCH₃)₂** is stable and the structure of which remains intact, while the **UiO-66-(SH)₂** may be oxidized and/or destructed under irradiation due to the sensitive –SH presented.

Photocatalytic activity of Pt/**UiO-66-(SCH₃)₂** to split water into H_2 by use alternative electron sacrificial reagents such as methanol and L-ascorbic acid were also observed. In 20 vol% methanolic aqueous solution, the highest H_2 production rate of Pt/**UiO-66-(SCH₃)₂** with 1.5 wt% platinum co-catalyst is 19 $umol \cdot g^{-1} h^{-1}$ under irradiation $\lambda > 400$ nm, being triple of that 6.96 $\mu mol\, g^{-1} h^{-1}$ for the case of TEOA reagent above. While, for the case of 0.1 M sacrificial ascorbic acid used, the maximum H_2 evolution rate reached 320 $umol \cdot g^{-1} h^{-1}$ after one hours under the same conditions (Fig. 5c). Except for that sharp comparison to that incapable photoactivity of UiO-66-NH_2 ($\lambda > 400$ nm), such value even is comparable to that 366.7 $\mu mol\, g^{-1} h^{-1}$ of the known Pt/MIL-125-NH_2 derived from aminoterephthalate linkers and Ti(IV)-oxo clusters [6d]. This H_2 evolution rate also is comparable to that of the analogous mixed-metal complex Pt/UiO-66(Zr/Ti)-NH_2 (370 $\mu mol\, g^{-1} h^{-1}$) of the UiO-66 family at the same condition [21]. Although the band gap energy (E_g) of UiO-66-NH_2 (2.72 eV) is comparable to that of **UiO-66-(SCH₃)₂** (2.80 eV), the photocatalytic activities between them are markedly different. This fact may be

ascribed to the distinct molecule dimensions and geometries of $-SCH_3$ and $-NH_2$ that exhibit different effects on the aromatic ring of the terephthalate linkers of the UiO-66 framework.

To investigate the concentration effect of the sacrificial ascorbic acid on the **Pt/UiO-66-(SCH₃)₂**, L-ascorbic acid from 0.1 M to 0.5 M (pH = 2.16 ~ 2.54) were used. The maximum H_2 generation after 3 h reached 3871 μmol/g at 0.2 M (PH = 2.37), and then gradually decreased with the concentration increasing (Fig. 6a). After 3 cycles test, the hydrogen production rate showed almost no decay for 0.2 M ascorbic acid case (Fig. 6b). Unchanged PXRD patterns of samples before and after reactions suggest the **UiO-66-(SCH₃)₂** is better solid photocatalyst (Fig. 5d). The further investigation on the acid/alkali-resistant ability of **UiO-66-(SCH₃)₂** showed that it is stable within a wide pH value (0 ~ 12) (Fig. 5d), exhibiting potential applications in harsh conditions. The fact is consistent with that unchanged PXRD patterns of **Pt/UiO-66-(SCH₃)₂** after reaction with the 0.1 vol% TEOA (pH = 7.20) as electronic sacrificial reagent (Fig. 5b). The preserved characteristic peak (around 2934 cm^{-1}) for the C−H vibration band of $−CH_3$ group infers the BDC-$(SCH_3)_2$ linkers remained intact on the **Pt/UiO-66-(SCH₃)₂** after reaction (Fig. 2a).

3. Conclusion

To sum up, sulfur-containing groups (X = $−SCH_3$, $−SH$, $−SO_3H$) with different electronic properties, molecule dimensions and geometries were used to modify the terephthalate linkers of UiO-66, obtaining isostructural complexes UiO-66-X_2 that act as n-type semiconductors with distinct photocatalytic properties. The electron-donating ability, molecular dimensions and geometry of the $− X$ groups play key roles in
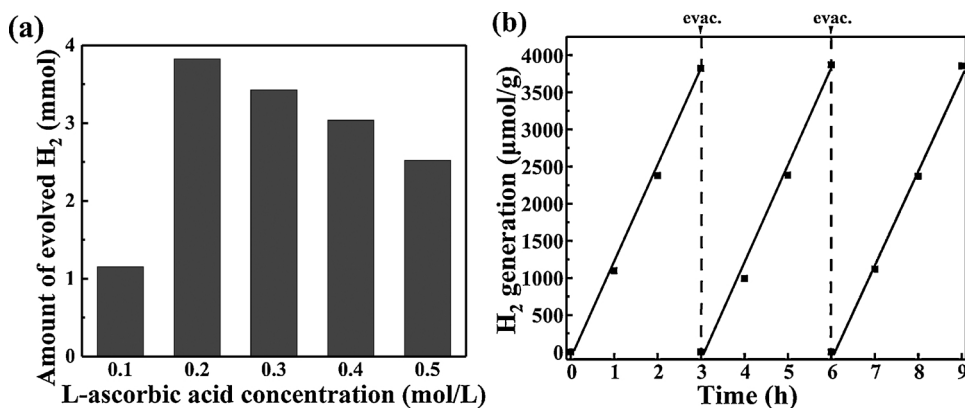
Fig. 6. (a) H_2 generation of **Pt/UiO-66-(SCH$_3$)$_2$** (1.5 wt% Pt) under irradiation of $\lambda > 400\,nm$ for 3 h with different concentrations of ascorbic acid. (b) Recycle test. Time course of hydrogen evolution over **Pt/UiO-66-(SCH$_3$)$_2$** in 0.2 M ascorbic acid for 9 h, with intermittent evacuation and exposure to atmospheric conditions every 3 h.

determining the band gap of the photocatalytic UiO-66-X$_2$. –SH and –SCH$_3$ are shown as the beneficial groups to improve the MOF's photocatalytic activity. The $-$ SCH$_3$ is the most efficient group to achieve the bathochromic shifting of the **UiO-66-(SCH$_3$)$_2$** and is responsible for that most large H_2 generation rate from water over the Pt/**UiO-66-(SCH$_3$)$_2$** catalyst under visible light irradiation. This work sheds some light on the tuning of the photoactive property of Zr(IV)-UiO-66 system by use sulfur-containing groups on the terephthalate linker, and other more MOFs functionalized with the –SCH$_3$ group are worthy of further exploring.

Declaration of Competing Interest

The authors declare that they have no known competing financial interests or personal relationships that could have appeared to influence the work reported in this paper.

Appendix A. Supplementary data

Supplementary material related to this article can be found, in the online version, at doi:https://doi.org/10.1016/j.apcatb.2019.118047.

References

[1] (a) X. Xu, C. Randorn, P. Efstathiou, J.T. Irvine, A red metallic oxide photocatalyst, Nat. Mater. 11 (2012) 595–598, https://doi.org/10.1038/NMAT3312;
(b) S. Chu, A. Majumdar, Opportunities and challenges for a sustainable energy future, Nature 488 (2012) 294–303, https://doi.org/10.1038/nature11475;
(c) X. Chen, L. Liu, P.Y. Yu, S.S. Mao, Increasing solar absorption for photocatalysis with black hydrogenated titanium dioxide nanocrystals, Science 331 (2011) 746–750, https://doi.org/10.1126/science.1200448;
(d) A. Fujishima, K. Honda, Electrochemical photolysis of water at a semiconductor electrode, Nature 238 (1972) 37–38, https://doi.org/10.1038/238037a0;
(e) J. Gao, J. Miao, P.Z. Li, W.Y. Teng, L. Yang, Y. Zhao, B. Liu, Q. Zhang, A p-type Ti(IV)-based metal-organic framework with visible-light photoresponse, Chem. Commun. (Camb.) 50 (2014) 3786–3788, https://doi.org/10.1039/c3cc49440c;
(f) F. Zuo, K. Bozhilov, R.J. Dillon, L. Wang, P. Smith, X. Zhao, P. Feng, Active facets on titanium(III)-Doped TiO$_2$: an effective strategy to improve the visible-light photocatalytic activity, Angew. Chem. Int. Ed 51 (2012) 6223–6226, https://doi.org/10.1002/anie.201202191.
[2] (a) M.A. Nasalevich, M. van der Veen, F. Kapteijn, J. Gascon, Metal-organic frameworks as heterogeneous photocatalysts: advantages and challenges, CrystEngComm 16 (2014) 4919, https://doi.org/10.1039/c4ce00032c;
(b) M.D. Hernández-Alonso, F. Fresno, S. Suárez, J.M. Coronado, Development of alternative photocatalysts to TiO2: challenges and opportunities, Energy Environ.

Sci. 2 (2009) 1231–1257, https://doi.org/10.1039/b907933e.
[3] (a) Z. Zou, J. Ye, K. Sayama, H. Arakawa, Direct splitting of water under visible light irradiation with an oxide semiconductor photocatalyst, Nature 414 (2001) 625–627;
(b) A. Kudo, Y. Miseki, Heterogeneous photocatalyst materials for water splitting, Chem. Soc. Rev. 38 (2009) 253–278, https://doi.org/10.1039/b800489g;
(c) H. Liu, J. Zhang, D. Ao, Construction of heterostructured ZnIn$_2$S$_4$@NH$_2$-MIL-125(Ti) nanocomposites for visible-light-driven H$_2$ production, Appl. Catal. B: Environ. 221 (2018) 433–442, https://doi.org/10.1016/j.apcatb.2017.09.043;
(d) P. Chowdhury, H. Gomaa, A.K. Ray, Dye-sensitized photocatalyst: a breakthrough in green energy and environmental detoxification, ACS Symp. Ser. 1124 (2013) 231–266, https://doi.org/10.1021/bk-2013-1124.ch013;
(e) R. Wang, L. Gu, J. Zhou, X. Liu, F. Teng, C. Li, Y. Yuan, Quasi-polymeric metal-organic framework UiO-66/g-C$_3$N$_4$ heterojunctions for enhanced photocatalytic hydrogen evolution under visible light irradiation, Adv. Mater. Interfaces 2 (2015) 1500037, , https://doi.org/10.1002/admi.201500037;
(f) D. Beydoun, R. Amal, G. Low, S. McEvoy, Role of nanoparticles in photocatalysis, J. Nanopart. Res. 1 (1999) 439–458;
(g) L. Shen, M. Luo, Y. Liu, R. Liang, F. Jing, L. Wu, Noble-metal-free MoS2 co-catalyst decorated UiO-66/CdS hybrids for efficient photocatalytic H$_2$ production, Appl. Catal. B: Environ. 166-167 (2015) 445–453, https://doi.org/10.1016/j. apcatb.2014.11.056.
[4] (a) P.-Q. Liao, X.-W. Chen, S.-Y. Liu, X.-Y. Li, Y.-T. Xu, M.-N. Tang, Z.-B. Rui, H.-B. Ji, J.-P. Zhang, X.-M, Putting an ultrahigh concentration of amine groups into a metal-organic framework for CO$_2$ capture at low pressures, Chen, Chem. Sci 7 (2016) 6528–6533, https://doi.org/10.1039/c6sc00836d;
(b) A. Schoedel, M. Li, D. Li, M. O'Keeffe, O.M. Yaghi, Structures of metal-organic frameworks with rod secondary building units, Chem. Rev. 116 (2016) 12466–12535, https://doi.org/10.1021/acs.chemrev.6b00346;
(c) H.-C. Zhou, S. Kitagawa, Metal-organic frameworks (MOFs), Chem. Soc. Rev. 43 (2014) 5415–5418, https://doi.org/10.1039/c4cs90059f;
(d) Y.J. Cheng, R. Wang, S. Wang, X.J. Xi, L.F. Ma, S.Q. Zang, Encapsulating [Mo$_3$S$_{13}$]$^{2-}$ clusters in cationic covalent organic frameworks: enhancing stability and recyclability by converting a homogeneous photocatalyst to a heterogeneous photocatalyst, Chem. Commun. (Camb.) 54 (2018) 13563–13566, https://doi.org/10.1039/C8CC07784C;
(e) T. Zhang, W. Lin, Metal-organic frameworks for artificial photosynthesis and photocatalysis, Chem. Soc. Rev. 43 (2014) 5982–5993, https://doi.org/10.1039/c4cs00103f;
(e.) Y. Chen, X. Huang, S. Zhang, S. Li, S. Cao, X. Pei, J. Zhou, X. Feng, B. Wang, Shaping of metal-organic frameworks: from fluid to shaped bodies and robust foams, J. Am. Chem. Soc. 138 (2016) 10810–10813, https://doi.org/10.1021/jacs. 6b06959;
(f) Q. Yang, Q. Xu, H.L. Jiang, Metal-organic frameworks meet metal nanoparticles: synergistic effect for enhanced catalysis, Chem. Soc. Rev. 46 (2017) 4774–4808, https://doi.org/10.1039/c6cs00724d;
(g) X.G. Yang, L.F. Ma, D.P. Yan, Facile synthesis of 1D organic–inorganic perovskite micro-belts with high water stability for sensing and photonic applications, Chem. Sci. 10 (2019) 4567–4572, https://doi.org/10.1039/C9SC00162J.
[5] (a) M. Alvaro, E. Carbonell, B. Ferrer, F.X. Llabrési Xamena, H. Garcia, Semiconductor behavior of a metal-organic framework (MOF), Chem. Eur. J. 13 (2007) 5106–5112, https://doi.org/10.1002/chem.200601003;
(b) T. Tachikawa, J.R. Choi, M. Fujitsuka, T. Majima, Photoinduced charge-transfer processes on MOF-5 nanoparticles: elucidating differences between metal-organic frameworks and semiconductor metal oxides, J. Phys. Chem. C 112 (2008) 14090–14101, https://doi.org/10.1021/jp803620v;
(c) Y. Lee, S. Kim, J.K. Kang, S.M. Cohen, Photocatalytic CO$_2$ reduction by a mixed metal (Zr/Ti), mixed ligand metal-organic framework under visible light irradiation, Chem. Commun. (Camb.) 51 (2015) 5735–5738, https://doi.org/10.1039/c5cc00686d;
(d) J. Gao, J. Miao, P.Z. Li, W.Y. Teng, L. Yang, Y. Zhao, Q. Zhang, A p-type Ti(IV)-based metal-organic framework with visible-light photoresponse, Chem. Commun. (Camb.) 50 (2014) 3786–3788, https://doi.org/10.1039/c3cc49440c;
(e) Y.B. Huang, J. Liang, X.S. Wang, Multifunctional metal-organic framework

catalysts: synergistic catalysis and tandem reactions, Chem. Soc. Rev. 46 (2017) 126–157, https://doi.org/10.1039/c6cs00250a;

(f) Q. Yang, Q. Xu, H.L. Jiang, Metal-organic frameworks meet metal nanoparticles: synergistic effect for enhanced catalysis, Chem. Soc. Rev. 46 (2017) 4774–4808, https://doi.org/10.1039/c6cs00724d;

(g) X.Y. Dong, M. Zhang, R.B. Pei, Q. Wang, D.H. Wei, S.Q. Zang, T.C. Mak, Crystalline copper(II) coordination polymer for the efficient visible-light-driven generation of hydrogen, Angew. Chem. Int. Ed. 55 (2016) 2073–2077, https://doi.org/10.1002/anie.201509744.

[6] (a) C. Gomes Silva, I. Luz, F.X. LiabrésiXamena, A. Corma, H. García, Water stable Zr-benzenedicarboxylate metal-organic frameworks as photocatalysts for hydrogen generation, Chem. Eur. J. 16 (2010) 11133–11138, https://doi.org/10.1002/chem.200903526;

(b) J.H. Cavka, S. Jakobsen, U. Olsbye, N. Guillou, C. Lamberti, S. Bordiga, K.P. Lillerud, A new zirconium inorganic building brick forming metal organic frameworks with exceptional stability, J. Am. Chem. Soc. 130 (2008) 13850–13851, https://doi.org/10.1021/ja8057953;

(c) Y. Fu, D. Sun, Y. Chen, R. Huang, Z. Ding, X. Fu, Z. Li, An amine-functionalized titanium metal-organic framework photocatalyst with visible-light-induced activity for CO_2 reduction, Angew. Chem. Int. Ed 51 (2012) 3364–3367, https://doi.org/10.1002/anie.201108357;

(d) Y. Horiuchi, T. Toyao, M. Saito, K. Mochizuki, M. Iwata, H. Higashimura, M. Matsuoka, Visible-Light-Promoted Photocatalytic Hydrogen Production by Using an Amino-Functionalized Ti(IV) Metal-Organic Framework, J. Phys. Chem. C. 116 (2012) 20848–20853, https://doi.org/10.1021/jp3046005;

(e) X. Wang, X. Zhao, D. Zhang, G. Li, H. Li, Microwave irradiation induced UIO-66-NH_2 anchored on graphene with high activity for photocatalytic reduction of CO_2, Appl. Catal. B: Environ. 228 (2018) 47–53, https://doi.org/10.1016/j.apcatb.2018.01.066;

(f) X. Li, Z. Le, X. Chen, Z. Li, W. Wang, X. Liu, A. Wu, P. Xu, D. Zhang, Graphene oxide enhanced amine-functionalized titanium metal organic framework for visible-light-driven photocatalytic oxidation of gaseous pollutants, Appl. Catal. B Environ. 236 (2018) 501–508, https://doi.org/10.1016/j.apcatb.2018.05.052.

[7] (a) L. Shen, R. Liang, M. Luo, F. Jing, L. Wu, Electronic effects of ligand substitution on metal-organic framework photocatalysts: the case study of UiO-66, Phys. Chem. Chem. Phys. 17 (2015) 117–121, https://doi.org/10.1039/c4cp04162c;

(b) E. Flage–Larsen, A. Røyset, J.H. Cavka, K. Thorshaug, Band gap modulations in UiO metal-organic frameworks, J. Phys. Chem. C. 117 (2013) 20610–20616, https://doi.org/10.1021/jp405335q;

(c) K. Hendrickx, D.E.P. Vanpoucke, K. Leus, K. Lejaeghere, A. Van Yperen-De Deyne, V. Van Speybroeck, K. Hemelsoet, Understanding intrinsic light absorption properties of UiO-66 frameworks: a combined theoretical and experimental study, Inorg. Chem. 54 (2015) 10701–10710, https://doi.org/10.1021/acs.inorgchem.5b01593.

[8] S.-Y. Han, D.-L. Pan, H. Chen, X.-B. Bu, Y.X. Gao, H. Gao, Y. Tian, G.-S. Li, G. Wang, S.-Li Cao, C.-Q. Wan, G.-C. Guo, A methylthio-functionalized-MOF Photocatalyst with high performance for visible-light-driven H_2 evolution, Angew. Chem. Int. Ed 57 (2018) 9864–9869, https://doi.org/10.1002/anie.201806077.

[9] (a) Yuan H. Zhao, Michael H. Abraham, Andreas M. Zissimos, Fast calculation of van der waals volume as a sum of atomic and bond contributions and its application to drug compounds, J. Org. Chem. 68 (2003) 7368–7373, https://doi.org/10.1021/jo034808o;

(b) L. Valenzano, B. Civalleri, S. Chavan, S. Bordiga, M.H. Nilsen, S. Jakobsen, K.P. Lillerud, C. Lamberti, Disclosing the complex structure of UiO-66 metal organic framework: a synergic combination of experiment and theory, Chem. Mater. 23 (2011) 1700–1718, https://doi.org/10.1021/cm1022882.

[10] (a) A. Dhakshinamoorthy, A.M. Asiri, H. Garcia, Catalysis by metal organic frameworks in water, Chem. Commun. (Camb.) 50 (2014) 12800–12814, https://doi.org/10.1039/c4cc04387a;

(b) C. Gomes Silva, I. Luz, F.X. Llabres i Xamena, A. Corma, H. Garcia, Water stable Zr-benzenedicarboxylate metal-organic frameworks as photocatalysts for hydrogen generation, Chem. 16 (2010) 11133–11138, https://doi.org/10.1002/chem.200903526.

[11] (a) L. Vial, R.F. Ludlow, J. Leclaire, R. Pérez-Fernández, S. Otto, Controlling the biological effects of spermine using a synthetic receptor, J. Am. Chem. Soc. 128 (2006) 10253–10257, https://doi.org/10.1021/ja062536b;

(b) K.K. Yee, N. Reimer, J. Liu, S.Y. Cheng, S.M. Yiu, J. Weber, N. Stock, Z. Xu, Effective mercury sorption by thiol-laced metal-organic frameworks: in strong acid and the vapor phase, J. Am. Chem. Soc. 135 (2013) 7795–7798, https://doi.org/10.1021/ja400212k.

[12] W.J. Phang, H. Jo, W.R. Lee, J.H. Song, K. Yoo, B. Kim, C.S. Hong, Superprotonic conductivity of a UiO-66 framework functionalized with sulfonic acid groups by facile postsynthetic oxidation, Angew. Chem. Int. Ed. 54 (2015) 5142–5146, https://doi.org/10.1002/anie.201411703.

[13] S. Parra, J. Olivero, L. Pacheco, C. Pulgarin, Structural properties and photo-reactivity relationships of substituted phenols in TiO_2 suspensions, Appl. Catal. B Environ. 43 (2003) 293–301, https://doi.org/10.1016/S0926-3373(02)00324-7.

[14] A.V. Krukau, O.A. Vydrov, A.F. Izmaylov, G.E. Scuseria, Influence of the exchange screening parameter on the performance of screened hybrid functionals, J. Chem. Phys. 125 (2006) 224106–224112, https://doi.org/10.1063/1.2404663.

[15] T.M. Henderson, J. Paier, G.E. Scuseria, Accurate treatment of solids with the HSE screened hybrid, Phys. Status Solidi B 248 (2011) 767–774, https://doi.org/10.1002/pssb.201046303.

[16] M.F. Peintinger, D.V. Oliveira, T. Bredow, Consistent Gaussian basis sets of Triple-Zeta valence with polarization quality for solid-State Calculations, J. Comput. Chem. 34 (2013) 451–459, https://doi.org/10.1002/jcc.23153.

[17] J. Laun, D.V. Oliveira, T. Bredow, Consistent gaussian basis sets of double-and triple-zeta valence with polarization quality of the fifth period for solid-state calculations, J. Comput. Chem. 39 (2018) 1285–1290, https://doi.org/10.1002/jcc.25195.

[18] R. Dovesi, V.R. Saunders, C. Roetti, R. Orlando, C.M. Zicovich-Wilson, F. Pascale, B. Civalleri, K. Doll, N.M. Harrison, I.J. Bush, Ph. D'Arco, M. Llunell, M. Causà, Y. Noël, CRYSTAL14 User's Manual, University of Torino, Torino, 2014.

[19] (a) M. Ye, J. Gong, Y. Lai, C. Lin, Z. Lin, High-efficiency photoelectrocatalytic hydrogen generation enabled by palladium quantum dots-sensitized TiO_2 nanotube arrays, J. Am. Chem. Soc. 134 (2012) 15720–15723, https://doi.org/10.1021/ja307449z;

(b) R. O'Hayre, M. Nanu, J. Schoonman, A. Goossens, Mott-Schottky and charge-transport analysis of nanoporous titanium dioxide films in air, J. Phy. Chem. C. 111 (2007) 4809–4814, https://doi.org/10.1021/jp068354l;

(c) Z. Zhang, Y. Yu, P. Wang, Hierarchical Top-Porous/Bottom-Tubular TiO_2 nanostructures decorated with Pd nanoparticles for efficient photoelectrocatalytic decomposition of synergistic pollutants, ACS Appl. Mater. Interfaces 4 (2012) 990–996, https://doi.org/10.1021/am201630s.

[20] T. Toyao, M. Saito, Y. Horiuchi, K. Mochizuki, M. Iwata, H. Higashimura, M. Matsuoka, Efficient hydrogen production and photocatalytic reduction of nitrobenzene over a visible-light-responsive metal-organic framework photocatalyst, Catal. Sci. Technol. 3 (2013) 2092–2097, https://doi.org/10.1039/c3cy00211j.

[21] D. Sun, W. Liu, M. Qiu, Y. Zhang, Z. Li, Introduction of a mediator for enhancing photocatalytic performance via post-synthetic metal exchange in metal-organic frameworks (MOFs), Chem. Commun. (Camb.) 51 (2015) 2056–2059, https://doi.org/10.1039/c4cc09407g.